Real-time eye motion compensation for OCT imaging with tracking SLO

Kari V. Vienola,[1,*] Boy Braaf,[1] Christy K. Sheehy,[2] Qiang Yang,[3] Pavan Tiruveedhula,[2] David W. Arathorn,[3] Johannes F. de Boer,[1,4] and Austin Roorda[2]

[1]*Rotterdam Ophthalmic Institute, Schiedamse Vest 160, 3011 BH Rotterdam, Netherlands*
[2]*School of Optometry, University of California, Berkeley; Berkeley, CA, 94720, USA*
[3]*Montana State University, Bozeman, MT 59717, USA*
[4]*LaserLAB, Department of Physics and Astronomy, VU University, de Boelelaan 1081, 1081 HV, Amsterdam, Netherlands*
*k.vienola@eyehospital.nl

Abstract: Fixational eye movements remain a major cause of artifacts in optical coherence tomography (OCT) images despite the increases in acquisition speeds. One approach to eliminate the eye motion is to stabilize the ophthalmic imaging system in real-time. This paper describes and quantifies the performance of a tracking OCT system, which combines a phase-stabilized optical frequency domain imaging (OFDI) system and an eye tracking scanning laser ophthalmoscope (TSLO). We show that active eye tracking minimizes artifacts caused by eye drift and micro saccades. The remaining tracking lock failures caused by blinks and large saccades generate a trigger signal which signals the OCT system to rescan corrupted B-scans. Residual motion artifacts in the OCT B-scans are reduced to 0.32 minutes of arc (~1.6 μm) in an *in vivo* human eye enabling acquisition of high quality images from the optic nerve head and lamina cribrosa pore structure.

© 2012 Optical Society of America

OCIS codes: (110.0110) Imaging systems; (110.4500) Optical coherence tomography; (170.4460) Ophthalmic optics and devices; (170.4470) Ophthalmology.

References and links

1. D. Huang, E. A. Swanson, C. P. Lin, J. S. Schuman, W. G. Stinson, W. Chang, M. R. Hee, T. Flotte, K. Gregory, C. A. Puliafito, and J. G. Fujimoto, "Optical coherence tomography," Science **254**(5035), 1178–1181 (1991).
2. W. Drexler and J. G. Fujimoto, "State-of-the-art retinal optical coherence tomography," Prog. Retin. Eye Res. **27**(1), 45–88 (2008).
3. A. F. Fercher, C. K. Hitzenberger, G. Kamp, and S. Y. El-Zaiat, "Measurement of intraocular distances by backscattering spectral interferometry," Opt. Commun. **117**(1-2), 43–48 (1995).
4. M. Wojtkowski, V. J. Srinivasan, T. H. Ko, J. G. Fujimoto, A. Kowalczyk, and J. S. Duker, "Ultrahigh-resolution, high-speed, Fourier domain optical coherence tomography and methods for dispersion compensation," Opt. Express **12**(11), 2404–2422 (2004).
5. R. Leitgeb, C. Hitzenberger, and A. Fercher, "Performance of fourier domain vs. time domain optical coherence tomography," Opt. Express **11**(8), 889–894 (2003).
6. J. F. de Boer, B. Cense, B. H. Park, M. C. Pierce, G. J. Tearney, and B. E. Bouma, "Improved signal-to-noise ratio in spectral-domain compared with time-domain optical coherence tomography," Opt. Lett. **28**(21), 2067–2069 (2003).
7. M. Choma, M. Sarunic, C. Yang, and J. Izatt, "Sensitivity advantage of swept source and Fourier domain optical coherence tomography," Opt. Express **11**(18), 2183–2189 (2003).
8. N. Nassif, B. Cense, B. Park, M. Pierce, S. Yun, B. Bouma, G. Tearney, T. Chen, and J. de Boer, "*In vivo* high-resolution video-rate spectral-domain optical coherence tomography of the human retina and optic nerve," Opt. Express **12**(3), 367–376 (2004).
9. N. Nassif, B. Cense, B. Hyle Park, S. H. Yun, T. C. Chen, B. E. Bouma, G. J. Tearney, and J. F. de Boer, "*In vivo* human retinal imaging by ultrahigh-speed spectral domain optical coherence tomography," Opt. Lett. **29**(5), 480–482 (2004).
10. S. Martinez-Conde, S. L. Macknik, and D. H. Hubel, "The role of fixational eye movements in visual perception," Nat. Rev. Neurosci. **5**(3), 229–240 (2004).

11. T. Klein, W. Wieser, C. M. Eigenwillig, B. R. Biedermann, and R. Huber, "Megahertz OCT for ultrawide-field retinal imaging with a 1050 nm Fourier domain mode-locked laser," Opt. Express **19**(4), 3044–3062 (2011).
12. B. Potsaid, I. Gorczynska, V. J. Srinivasan, Y. Chen, J. Jiang, A. Cable, and J. G. Fujimoto, "Ultrahigh speed spectral / Fourier domain OCT ophthalmic imaging at 70,000 to 312,500 axial scans per second," Opt. Express **16**(19), 15149–15169 (2008).
13. S. Ricco, M. Chen, H. Ishikawa, G. Wollstein, and J. Schuman, "Correcting motion artifacts in retinal spectral domain optical coherence tomography via image registration," Med Image Comput Comput Assist Interv **12**(Pt 1), 100–107 (2009).
14. M. F. Kraus, B. Potsaid, M. A. Mayer, R. Bock, B. Baumann, J. J. Liu, J. Hornegger, and J. G. Fujimoto, "Motion correction in optical coherence tomography volumes on a per A-scan basis using orthogonal scan patterns," Biomed. Opt. Express **3**(6), 1182–1199 (2012).
15. D. A. Robinson, "A method of measuring eye movement using a scleral search coil in a magnetic field," IEEE Trans. Biomed. Eng. **10**, 137–145 (1963).
16. H. D. Crane and C. M. Steele, "Generation-V dual-Purkinje-image eyetracker," Appl. Opt. **24**(4), 527–537 (1985).
17. T. N. Cornsweet and H. D. Crane, "Accurate two-dimensional eye tracker using first and fourth Purkinje images," J. Opt. Soc. Am. **63**(8), 921–928 (1973).
18. R. W. Ditchburn and B. L. Ginsborg, "Involuntary eye movements during fixation," J. Physiol. **119**(1), 1–17 (1953).
19. T. N. Cornsweet, "New technique for the measurement of small eye movements," J. Opt. Soc. Am. **48**(11), 808–811 (1958).
20. R. H. Webb and G. W. Hughes, "Scanning laser ophthalmoscope," IEEE Trans. Biomed. Eng. **BME-28**(7), 488–492 (1981).
21. R. H. Webb, G. W. Hughes, and F. C. Delori, "Confocal scanning laser ophthalmoscope," Appl. Opt. **26**(8), 1492–1499 (1987).
22. J. B. Mulligan, "Recovery of motion parameters from distortions in scanned images," in *Proceedings of the NASA Image Registration Workshop (IRW97)* (NASA Goddard Space Flight Center, MD, 1997), pp. 281–292.
23. M. Stetter, R. A. Sendtner, and G. T. Timberlake, "A novel method for measuring saccade profiles using the scanning laser ophthalmoscope," Vision Res. **36**(13), 1987–1994 (1996).
24. D. P. Wornson, G. W. Hughes, and R. H. Webb, "Fundus tracking with the scanning laser ophthalmoscope," Appl. Opt. **26**(8), 1500–1504 (1987).
25. R. D. Ferguson, D. X. Hammer, L. A. Paunescu, S. Beaton, and J. S. Schuman, "Tracking optical coherence tomography," Opt. Lett. **29**(18), 2139–2141 (2004).
26. D. Hammer, R. D. Ferguson, N. Iftimia, T. Ustun, G. Wollstein, H. Ishikawa, M. Gabriele, W. Dilworth, L. Kagemann, and J. Schuman, "Advanced scanning methods with tracking optical coherence tomography," Opt. Express **13**(20), 7937–7947 (2005).
27. R. D. Ferguson, "Servo tracking system utilizing phase-sensitive detection of reflectance variations," U.S. patent 5,943,115 (August 24, 1999).
28. B. Braaf, K. A. Vermeer, V. A. D. P. Sicam, E. van Zeeburg, J. C. van Meurs, and J. F. de Boer, "Phase-stabilized optical frequency domain imaging at 1-μm for the measurement of blood flow in the human choroid," Opt. Express **19**(21), 20886–20903 (2011).
29. C. K. Sheehy, Q. Yang, D. W. Arathorn, P. Tiruveedhula, J. F. de Boer, and A. Roorda, "High-speed, image-based eye tracking with a scanning laser opthalmoscope," Biomed. Opt. Express **3**(10), 2611–2622 (2012).
30. D. R. Skinner and R. E. Whitcher, "Measurement of the radius of a high-power laser beam near the focus of a lens," J. Phys. E Sci. Instrum. **5**(3), 237–238 (1972).
31. J. M. Khosrofian and B. A. Garetz, "Measurement of a Gaussian laser beam diameter through the direct inversion of knife-edge data," Appl. Opt. **22**(21), 3406–3410 (1983).
32. Q. Yang, D. W. Arathorn, P. Tiruveedhula, C. R. Vogel, and A. Roorda, "Design of an integrated hardware interface for AOSLO image capture and cone-targeted stimulus delivery," Opt. Express **18**(17), 17841–17858 (2010).
33. S. B. Stevenson, A. Roorda, and G. Kumar, "Eye tracking with the adaptive optics scanning laser ophthalmoscope," in *ETRA '10 Proceedings of the 2010 Symposium on Eye-Tracking Research & Applications* (ACM, 2010), pp. 195–198.
34. J. M. Findlay, "Frequency analysis of human involuntary eye movement," Kybernetik **8**(6), 207–214 (1971).
35. M. Ezenman, P. E. Hallett, and R. C. Frecker, "Power spectra for ocular drift and tremor," Vision Res. **25**(11), 1635–1640 (1985).
36. J. B. Jonas, C. Y. Mardin, U. Schlötzer-Schrehardt, and G. O. Naumann, "Morphometry of the human lamina cribrosa surface," Invest. Ophthalmol. Vis. Sci. **32**(2), 401–405 (1991).
37. L. Dandona, H. A. Quigley, A. E. Brown, and C. Enger, "Quantitative regional structure of the normal human lamina cribrosa. A racial comparison," Arch. Ophthalmol. **108**(3), 393–398 (1990).
38. B. Braaf, K. A. Vermeer, K. V. Vienola, and J. F. de Boer, "Angiography of the retina and the choroid with phase-resolved OCT using interval-optimized backstitched B-scans," Opt. Express **20**(18), 20516–20534 (2012).
39. T. Torzicky, M. Pircher, S. Zotter, M. Bonesi, E. Götzinger, and C. K. Hitzenberger, "High-speed retinal imaging with polarization-sensitive OCT at 1040 nm," Optom. Vis. Sci. **89**(5), 585–592 (2012).

40. R. J. Zawadzki, S. M. Jones, S. S. Olivier, M. Zhao, B. A. Bower, J. A. Izatt, S. Choi, S. Laut, and J. S. Werner, "Adaptive-optics optical coherence tomography for high-resolution and high-speed 3D retinal *in vivo* imaging," Opt. Express **13**(21), 8532–8546 (2005).
41. L. J. Van Rijn, J. Van der Steen, and H. Collewijn, "Instability of ocular torsion during fixation: cyclovergence is more stable than cycloversion," Vision Res. **34**(8), 1077–1087 (1994).

1. Introduction

Optical coherence tomography (OCT) is an interferometric imaging modality that allows cross-sectional imaging of internal biological structures [1]. Since its invention, OCT has become a standard tool in ophthalmology to diagnose and study various eye diseases [2]. The noninvasive nature and high axial (3-5 µm) and lateral (5-30 µm) resolution are ideal to visualize the underlying structures and detect changes in the retinal tissue of healthy and diseased eyes. The emergence of spectral domain OCT [3,4], with a 100 to 1000 fold improvement in sensitivity [5–7] and the associated increase in scan speed allowing video rate imaging [8,9] has made a significant impact in the field.

However, during image acquisition the eye is constantly moving. These involuntary fixational eye movements (e.g., micro saccades and drift [10]) remain a major cause of artifacts in OCT images even in ultrahigh-speed systems [11,12]. Post-processing algorithms have been developed to remove eye motion [13,14], but large and rapid eye movement can cause gaps in volume imaging which cannot be corrected with post-processing. Further, eye motion causes distortions and complicates the averaging of multiple B-scans in order to enhance the signal-to-noise ratio (SNR).

Another approach to eliminate eye motion artifacts from the data is to monitor eye motion and correct the ophthalmic imaging system in real-time. Several methods have been developed over the years to track and quantify eye motion. The earliest methods measured motion of the anterior segment of the eye using magnetic search coils [15], movement of the reflection from the anterior optics [16,17] or were based on reflections from tight fitted contact lenses with tiny mirrors [18]. With the exception of the contact lens approach, these methods are still commonly used in many settings, but they are limited in the sense that the exact movement of the retina, and the associated retinal image, is never recorded directly.

The first retinal image-based tracker measured the lateral motion of a blood vessel with a simple line-scan camera [19]. This was a precursor to the scanning laser ophthalmoscope (SLO), invented by Webb *et al.* [20,21] which offered a completely new tool in eye imaging. The confocality of SLO allowed the capture of high quality *en face* videos of the retina. The advantages of SLO for eye tracking were appreciated early on and systems were soon described for tracking retinal motion by the frame rate [22] and analyzing distortions within sections of individual frames [23,24]. The latter concepts and technologies set the stage for the correction of motion artifacts that we report in this paper.

To overcome the problems that fixational eye movements cause in OCT imaging, several commercial systems have implemented eye tracking into their existing OCT devices e.g., Spectralis® OCT (Heidelberg Engineering, Germany), RTVue (Optovue Inc., USA) and tracking OCT from Physical Sciences Inc. (PSI) [25,26]. The Spectralis and RTVue systems use image-based tracking in which eye motions are extracted from video frames and the OCT beam is steered to keep it on target. In the Spectralis® system, the retinal image (1,000 points) from the infra-red SLO imaging channel is used to track motion. In the RTVue system the motion is measured at 30 Hz from an infrared full-field fundus camera. The PSI system uses a non-imaging method where a dithering beam is used to lock on reflectance changes from single retinal features within the optic nerve head (ONH) or on blood vessels [27]. The eye motion signal is used to control the OCT scanning mirrors to maintain the OCT scanning grid on its retinal target, except in the PSI system, where the beam is controlled with additional tracking mirrors.

In this paper we present our existing optical frequency domain imaging (OFDI) system [28] with implemented experimental tracking SLO (TSLO) [29]. The TSLO images the eye

with a frame rate of 30 Hz but extracts eye motion at much higher rates by analyzing distortions within sections of each captured frame. These extracted eye motion signals are transformed into tracking signals that are combined with the signals that drive the OCT galvo mirrors. We present a careful performance analysis emphasizing tracking and stabilization accuracy of the TSLO. Further, we present images of the retina and the ONH that are free from micro saccades and drift. Finally, we demonstrate how large and rapid saccades or blinks that lead to untracked motion can be corrected by implementing a validity signal to the OFDI-TSLO system that enables rescanning of the retinal areas where tracking was lost.

2. Experimental system

2.1. Optical setup

A detailed description of the OFDI system can be found in Braaf *et al.* [28] and optical layout can be seen in Fig. 1. It uses a 100 kHz swept-source (Axsun Technologies, USA) with a center wavelength of 1050 nm and an axial resolution of 4.8 μm (6.5 μm in air). For calibration and phase-stabilization a parallel, externally built Mach-Zehnder interferometer (illustrated as the MZI block in Fig. 1) is used to align A-lines to the same wave numbers (k-space) in post-processing. The beam diameter on the cornea was measured to be 1.62 mm ($1/e^2$) with a knife edge method [30,31]. The corresponding theoretical diffraction-limited spot size on the retina was calculated to be 13.7 μm.

  Technical details of the TSLO are described in Sheehy *et al.* [29] and the optical schematic is shown in Fig. 1. In summary, it uses a super luminescent diode (SLD-371, Superlum, Russia) with a center wavelength of 840 nm as the light source. The TSLO images the eye with 512×512 pixel frames acquired at 30 Hz over a field size of 4 degrees. A 16 kHz resonant scanner (Electro-Optical Products Corporation) is used for fast-axis (horizontal) scanning and slow-axis (vertical) scanning is performed by a galvo scanner at 30 Hz (Cambridge Technologies). The reflected light from the retina was detected with a photomultiplier tube (PMT). To provide tracking signals in real-time, the TSLO image
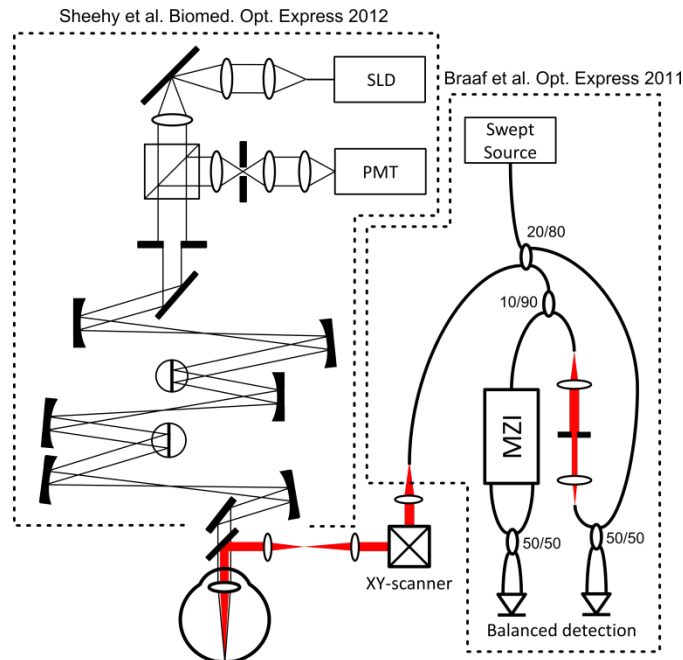

Fig. 1. A layout of the optical setup. SLD: Super luminescent diode; VS: Vertical scanner; HS: Horizontal Scanner; DM: Dichroic Mirror; PMT: Photomultiplier tube; MZI: external Mach-Zehnder Interferometer. The numbers are presenting the splitting ratios of the fiber couplers.

acquisition and processing was custom designed and uses the combined functionality of a GPU (GeForce GTX 560) and a Field-Programmable Gate Array (FPGA) board (Virtex 5, Xilinx).

The OFDI and TSLO systems were combined via a dichroic mirror and the layout of the optical setup is shown in Fig. 1. The optical power on the cornea was measured to be 1.48 mW (1050 nm) and 460 µW (840 nm), for which the combination was calculated to be within the ANSI standards for laser safety. The OCT sensitivity was measured to be 99.5 dB, which is 7.9 dB lower than the computed theoretical sensitivity of 107.4 dB. This decrease in sensitivity is due to optical losses in the sample arm and interferometer.

A schematic showing how the information flows is presented in Fig. 2. In short, the TSLO images the retina at 30 frames/s and the motion from the SLO frames is extracted taking advantage of the GPU and FPGA to deliver a high quality tracking signal with minimal latency. The tracking signal is the inverse of the eye motion scaled to fit the OCT galvo scanner voltage range. An electronic summing junction adds the tracking signal to the OCT galvo scanner steering signals (marked as + in Fig. 2). This voltage scaling is explained in section 3.2.
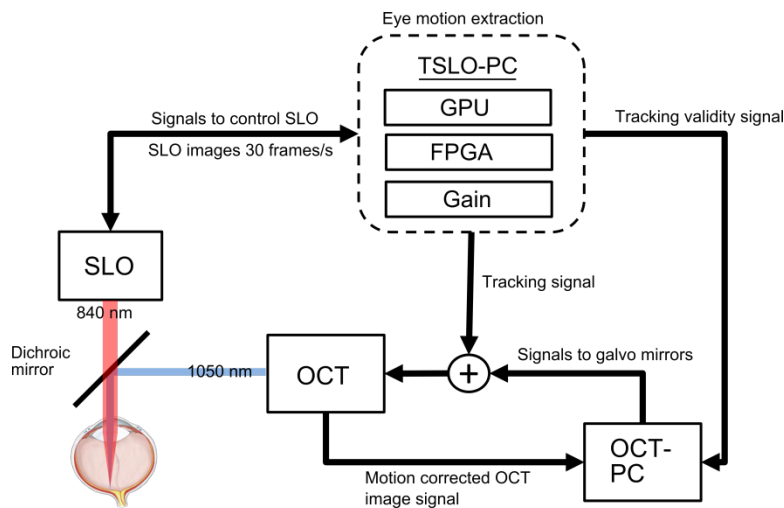

Fig. 2. An overview of the information flow. The TSLO images the retina at 30 frames/s and the eye motion is extracted in the TSLO-PC using the FPGA and GPU. The inverse eye motion signals are then scaled to match the voltage range in the OCT system (Gain). Tracking signals are combined with OCT beam steering signals in the electronic summing junction (+) to compensate for the eye motion in real-time. The tracking validity signal is used to indicate B-scans that need to be rescanned because tracking failures occurred due to large eye motions or blinks.

2.2. Image stabilization

The software that was used to extract the eye motion from TSLO images is similar to that described by Yang *et al.* [32] and Stevenson *et al.* [33] and is briefly explained here. First, a TSLO reference frame is selected. Then each consecutive frame is broken down into small strips which are cross-correlated one by one with the reference frame. The displacements of the strips in the horizontal and vertical directions provide the eye motion, which is inverted and used as correction signal for the OCT system. In the current setup, each frame is split into 32 overlapping strips, each 32 pixels high and 512 pixels wide, which yield an eye motion reporting rate of 960 Hz.

In the case of tracking failures, the TSLO-PC will send an invalid signal to the OCT-PC. Tracking failures are identified by sub threshold correlations of the current frame with the reference frame. Low correlations are caused by (i) large drifts, which limit the amount of

overlap between strips in the current frame and the reference frame, (ii) large saccades, which cause excessive shearing distortions of strips in the current frame, (iii) vertical motion, which leads to loss of overlap between strips in the current frame with the reference frame, (iv) blinks and (v) misalignments of the pupil, which cause reductions in image quality. Upon receiving the invalid signal, the OCT initiates rescanning of earlier B-scans, so that valid B-scans are acquired over the entire volume image. Specifically, after receiving the invalid signal, the OCT slow-axis scanner steps back 10 B-scans and waits for the validity signal to become valid again. When the validity signal indicates that the tracking is working again, the acquisition of B-scans is continued. B-scans that are corrupted by failed tracking are logged and then removed in post-processing.

2.3. Ethical considerations

The use of our experimental setup for *in vivo* measurements in humans was approved by the local Institutional Review Board and adhered to the tenets of the Declaration of Helsinki. Informed consent was obtained from each subject.

3. Tracking performance analysis

For reference, the amplitude spectrum of typical eye motion during fixation is presented in Fig. 3. This spectrum was generated using the same image-based algorithms to measure eye motion from SLO videos as described in section 2.2, but was done offline with a more robust and higher frequency analysis (64 strips per frame or 1920 Hz). The spectrum was computed from ten, 10-second videos recorded from an eye that was fixating. The spectrum shows that the frequencies of eye motion drop in a $1/f$ manner similar to that described in the literature [34]. Beyond 10 Hz, the amplitude of eye motion is generally less than 0.5 minutes of arc, which corresponds to approximately 2.4 µm in a normal eye. This spectrum establishes the frequencies and magnitudes that the TSLO should be designed to correct.
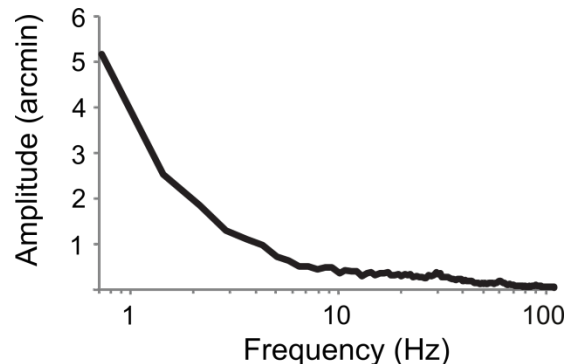

Fig. 3. The frequency spectrum of eye motion that was measured from a healthy volunteer (adapted from Sheehy *et al.* [29]). The spectrum shows similar behavior as reported in the literature [33–35].

3.1. Tracking OCT performance

TSLO performance was quantified by testing it on a model eye which was designed to simulate eye motion. The model eye consisted of a lens (f = 25 mm), an artificial retina made from translucent tape layers to provide texture in both lateral and axial directions and a galvanometer mirror (6200H, Cambridge Technologies, USA) in between. In the model eye, lateral motion of the retina was simulated by scanning the galvo mirror with variable frequency and amplitude. The motion generated in the model eye was typically faster and larger than the human eye naturally produces to test the TSLO under extreme conditions.

The motion of the model eye was sinusoidal and varied from 1 to 128 Hz. The amplitude was adjusted to be well above typical human eye motion but low enough to avoid tracking

failures caused by excessive image distortions. The motion of the model eye was calculated from SLO measurements with and without tracking to determine the motion correction performance. The percentage of correction was computed as 100% minus the output motion divided by input motion. More details on this step are described by Sheehy *et al.* [29].

In the OCT tracking application, there is an additional error caused by the time delay, or latency, between the motion measurement and applying the correction to the OCT scanners. The latency of the TSLO system was measured to be 2.5 ms, which was computed from measurements of the phase delay between the actual motion (derived from the position sensor) of the galvo scanner in the model eye and the correction signals sent from the TSLO to the OCT scanners.

Figure 4 shows the final performance of the motion correction for the OCT as a function of frequency, which was computed by combining the TSLO frequency performance (Sheehy *et al.* [29]) with the latency. The 50% (3 dB) motion correction bandwidth is just above 32 Hz which is sufficient to compensate most eye motion in a fixating eye.
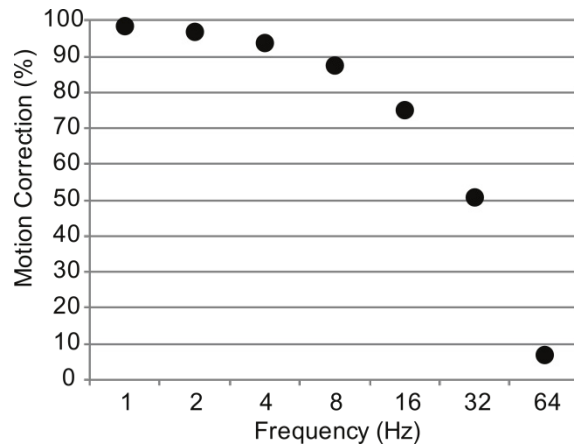

Fig. 4. The magnitude of motion correction of the TOCT as a function of frequency. The plot was generated from the eye motion measurement performance of the TSLO (Sheehy *et al.* [29]) combined with the additional error caused by the latency between the eye motion measurement and the output of correction signals to the OCT galvo scanners.

The velocity threshold of the eye motion for 4° field of view is approximately 14°/s [29]. Since saccades can have higher velocities than 14°/s [10], tracking failures caused by fast and large saccades do occur in the data sets. These failures will likely occur more frequently in inexperienced subjects and patients due to more saccadic motion during fixation. However, tracking failures are accounted for by the previously mentioned validity signal.

3.2. Scaling of the correction signals

An adjustable gain factor was added to the TSLO control software to correct for differences between the eye motion correction voltage outputs and the voltage response of the OCT scanners.

To determine the optimal gain value, we acquired a series of B-scans of the model eye with a large amplitude sinusoidal oscillation. With the tracking system on, we adjusted the gain until we found a minimum in the residual motion. To quantify the residual motion, the series of B-scans was cross-correlated to a reference frame (first acquired B-scan). Figure 5 shows the minimum residual motion achieved in the system when the input motion amplitude is ±17.4 minutes of arc at 1 Hz. The residual motion never reduced to zero because the B-scan continued to rock (tilt) in the axial direction even after motion correction, owing to the change in path length caused by the way we generated eye motion in the model eye. In addition to the tilt effect, the internal latency contributed to the residual motion. The amplitude of the fitted

sine curve is 0.5 arcmin and the lowest standard deviation (SD) of residual motion was found to be 0.37 minutes of arc. To make model eye motion comparable with the real eye motion, we took SD since eye motion is not periodic. In Fig. 4, 1 Hz motion is corrected by 98.4% which means that the residual sinusoidal motion amplitude from 17.4 arcmin should be 0.28 arcmin (1.6%). This value is in good agreement with the experimentally measured value.
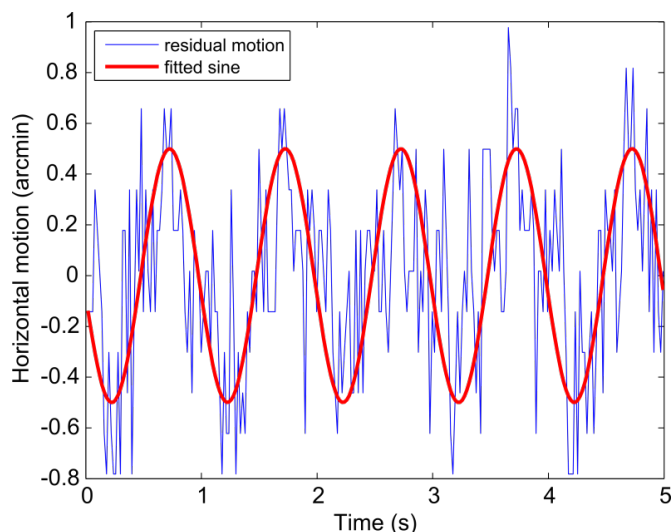

Fig. 5. Residual motion that is present in the OCT data after applying the optimal gain setting for eye motion compensation. The standard deviation is 0.37 minutes of arc, which corresponds to approximately 2.7 μm (as comparison the spot size on the human retina was calculated to be 13.7 μm).

4. Imaging

4.1. Performance of the TOCT imaging in the model eye

Before imaging human eyes, motion correction in tracking OCT was tested with the model eye. In Fig. 6, 250 B-scans were taken with and without tracking. The motion in the model eye was a 1 Hz sinusoidal wave that generated a ±12.4 arcmin movement of the artificial retina. Each acquired B-scan was integrated over depth and displayed in sequence to create what we term a B-scan trace for untracked (A) and tracked (B) imaging. Comparing the B-scan traces from Fig. 6 it is apparent that the motion is well compensated. Without tracking a clear 1 Hz sinusoidal motion is seen, whereas with tracking the features in the B-scan trace remain stationary, forming straight lines. This is quantified with cross-correlation to measure the motion within the series of B-scans. In Fig. 6(C) the horizontal motion is plotted as a function of time. Without tracking the SD of the motion is 8.27 arcmin and with tracking it reduces to 0.40 arcmin. This is consistent with the value obtained from the correction signal scaling experiment in section 3.2. The visible features in B-scan traces are from tape layers that were used to make the artificial retina.

In Fig. 7 a square area of the model retina was imaged under three different conditions using the same model eye as previously described. An *en face* image from each condition is presented. The left image shows the model retina imaged with no motion in the retina and tracking switched off (Fig. 7(A)). Figure 7(B) shows the motion artifacts when motion is induced and Fig. 7(C) shows how tracking corrects the motion while motion was put into the system. When comparing Figs. 7(A) and 7(C), it is seen that the original structure is recovered when tracking is enabled.
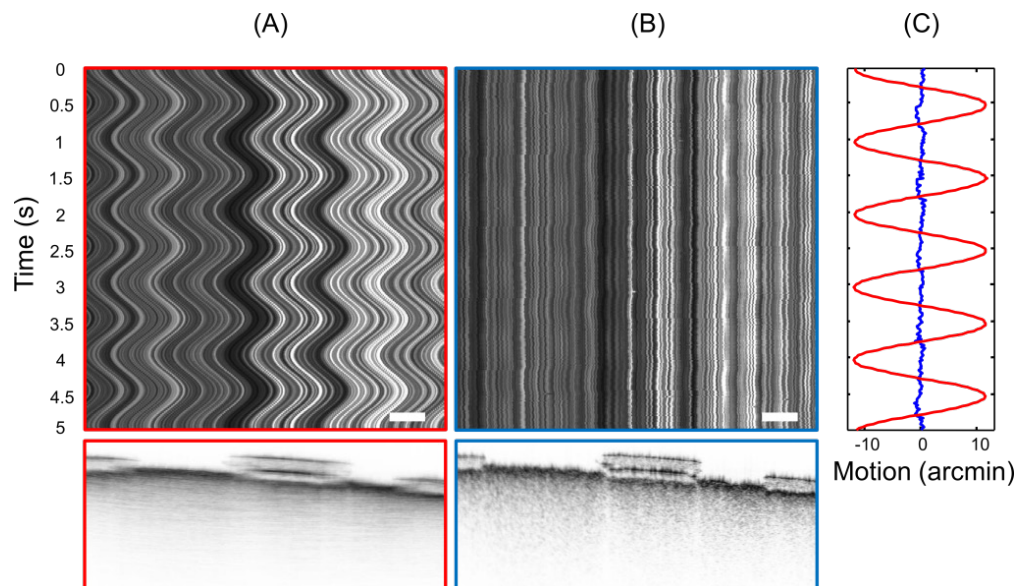
(A) (B) (C)

Fig. 6. B-scans taken from the model eye over the course of 5 seconds. (A) B-scans were taken without tracking and the features can be seen oscillating in the trace image. Below the image, all 250 frames were averaged which resulted in a blurry cross-sectional image of the tape layers in the artificial retina. (B) The same location was imaged with tracking. It is clearly seen that the previously seen motion is compensated. Again, below the image, all 250 frames were averaged together and this produced a cross-sectional image of the tape layers with clear structure. (C) The first frame from each data set was taken as reference frame and the consecutive frames were cross-correlated to the selected reference. In C the horizontal B-scan motion is plotted as a function of time. The red curve is derived from A (no tracking) and the blue curve from B (tracking). The standard deviation for the untracked curve is 8.3 arcmin and for tracked 0.4 arcmin. Scale bars indicate 0.5 deg.

(A) (B) (C)

No motion,
tracking OFF
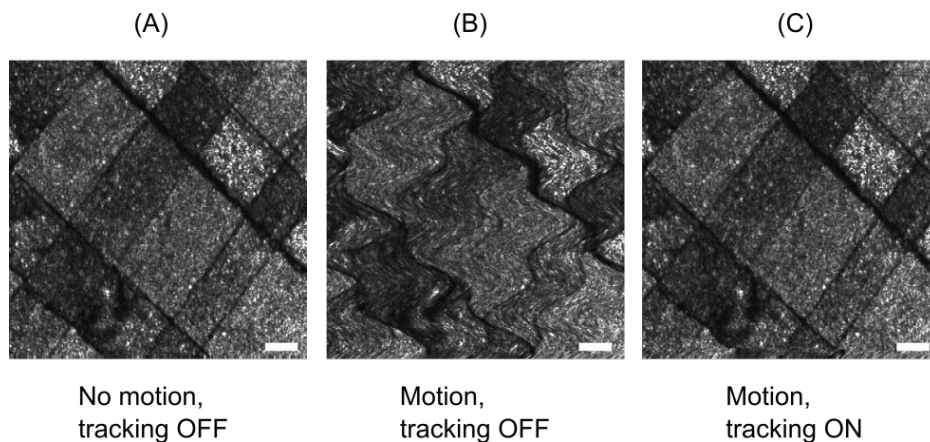
Motion,
tracking OFF

Motion,
tracking ON

Fig. 7. *En face* (B-scans integrated over depth) images of the model retina consisting of layers of tape under different conditions. (A) No motion is present and tracking signals are not generated. (B) System is introduced to a horizontal 1 Hz sinusoidal motion with an amplitude of ±12.4 arcmin, tracking is off. (C) Motion is the same as in B but tracking signals are generated and combined with OCT beam steering signals to compensate eye motion. In C it is seen that the original structure of the moving retina is recovered. Scale bars indicate 0.5 deg.

4.2. Performance of the TOCT imaging in a real eye

To measure the tracking stability in a human eye, 250 B-scans consisting of 2000 A-lines were acquired from the same location in a healthy volunteer. The SLO video recording was

triggered by the OCT data acquisition to synchronize data collection between the two imaging systems. The simultaneously acquired TSLO video was analyzed to determine the actual eye motion that took place during the acquisition of the OCT data set. The OCT measurement with this protocol took approximately 5 seconds. B-scan traces were generated with and without tracking (Fig. 8) in the same manner as for the model eye. In Fig. 8(A) the features in B-scan trace image (*en face* image) are changing as the eye moves. Lateral shifts of the B-scan trace match well with the TSLO eye motion trace that is located on the left side of the figure (blue trace), whereas vertical motion of the eye (green trace) causes the intensity profile of the B-scan to change over time. The OCT B-scan images were also used to estimate the lateral eye motion. Cross-correlation of the first B-scan image with subsequent B-scan images was used to calculate the lateral and axial displacement, where the axial motion was ignored. TSLO and OCT B-scan image motion analysis (shown on the left and right side of the B-scan trace, respectively) are in a good agreement. The standard deviation of the eye trace data is 4.7 arcmin for horizontal and 1.9 arcmin for vertical motion (vector sum being 5.1 arcmin). In
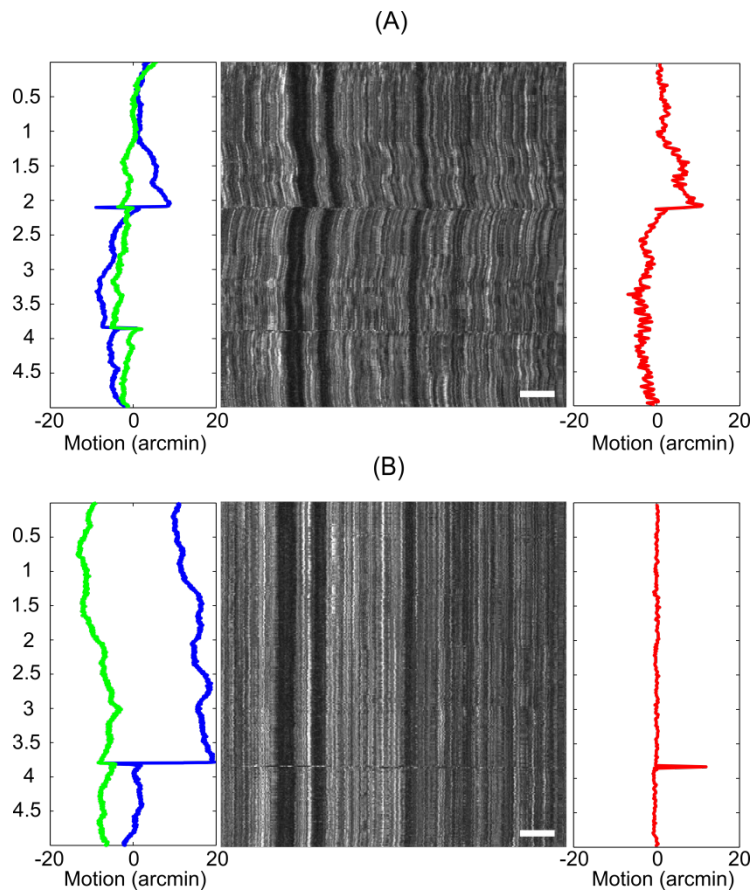

Fig. 8. B-scan trace image of 250 B-scans consisting of 2000 A-lines/B-scan taken without (A) and with (B) tracking. (A) The left graph shows the eye traces extracted from TSLO videos where blue is the horizontal motion and green is vertical. The B-scan trace image correlates with the blue curve (horizontal motion). On the right, a cross-correlation graph of the OCT data is plotted, which matches well with the TSLO horizontal eye trace. In the OCT cross-correlation plot, the first B-scan of the data set was taken as a reference frame and consecutive frames were cross-correlated against it. Only lateral motion was calculated, axial motion was ignored. (B) Same location as the area in (A) but with tracking. A large saccade is present that is seen as a peak in the cross-correlation curve and as a clear shift in the B-scan trace image. Scale bars indicate 0.5 deg.

Fig. 8(B) the same area is imaged as in Fig. 8(A) but with tracking enabled. The motion of the eye was similar to the previous measurement (6.8 arcmin horizontal, 2.6 arcmin vertical and vector sum 7.3 arcmin), but the standard deviation from the eye motion compensated cross-correlation data is reduced from 7.3 arcmin to 0.8 arcmin. This value is higher than shown in the model eye data (0.40 arcmin) due, in part, to a large (12 arcmin) untracked horizontal saccade that appeared in the data. If this saccade is removed from the data, the reduced motion gets a value of 0.32 arcmin.

The same subject was used to test the benefits of tracking on the acquisition of OCT volume images. To visualize the benefit, each acquired B-scan in a volume data set was integrated over depth to create an *en face* image. Actual eye motion traces were extracted from the simultaneously acquired TSLO video for each OCT volume. In Fig. 9 four different *en face* images are shown. Figures 9(A) and 9(B) are taken from an area of 3.11 × 3.11 mm
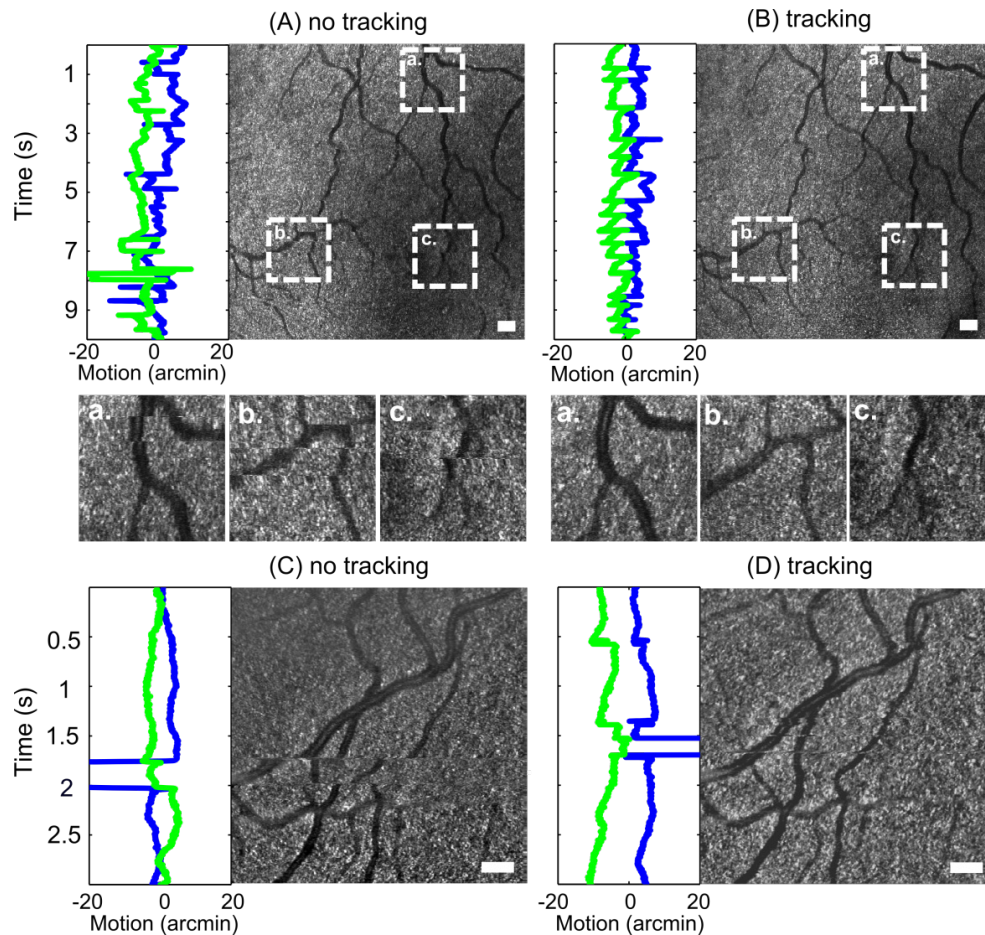

Fig. 9. *En face* images from 4 different volume data sets. (A) Large field of view (10.6° or 3.11 × 3.11 mm) was imaged without tracking enabled. On the left of the image A the corresponding eye traces are plotted. Below the image, three different areas are shown as zoomed versions from the large image. (B) Same area imaged as in A but tracking was enabled. Enlarged areas show that the motion artifacts are compensated. (C) The smaller field of view (5.3° or 1.56 × 1.56 mm) clearly demonstrates eye motion artifacts. One large saccade causes the scanning grid to acquire data from different position. (D) Same area imaged as in C but with tracking enabled. In this data set there is a large saccade which is tracked well. However, the final image still shows artifacts from brief tracking failures. To fully compensate large eye motions, a validity signal needs to be used to rescan the areas that are affected by improper tracking (see Fig. 10). Scale bars indicate 0.5 deg.

(10.6°) with a scanning protocol of 1000 B-scans, each consisting of 1000 A-lines. On the left side of each image the corresponding eye traces (blue = horizontal, green = vertical) are plotted. Three areas are zoomed to show how the motion distorts the vessel patterns and how with tracking these vessel patterns are undistorted. In Figs. 9(C) and 9(D) smaller areas were imaged with a field size of 1.56 × 1.56 mm (5.3°). Both images show a large saccade and with the tracked version the large eye motion is clearly compensated. Small distortions are still visible in the tracking image due to tracking failures. These distortions demonstrate the need to implement the validity signal to signal the OCT system to rescan these areas and to remove these distortions from the image.

As said, image distortions from large saccades and data gaps from blinks remain in the data set even when tracking is used. For these reasons, tracked volume scans with the validity signal (see section 2.2) were taken (700 B-scans, each consisting of 700 A-lines). In Fig. 10 two areas are shown of 2.2 × 2.2 mm (6.9°) and 2.7 × 2.7 mm (8.8°) from retinal vessels and the ONH respectively. The upper images show the whole data set, including the B-scans that are logged as corrupted. These corrupt B-scans are removed in the bottom images to generate a new *en face* image. The benefits of tracking and validity signal are clearly seen in these images.

Raw data with corrupted B-scans
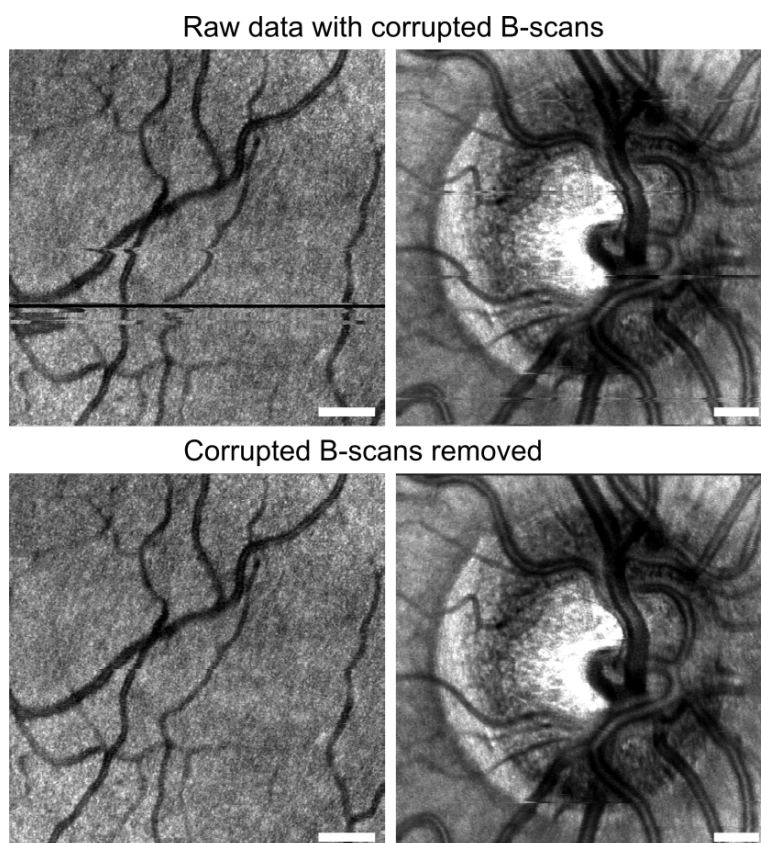

Corrupted B-scans removed

Fig. 10. Tracked *en face* images with validity signal. When tracking software lost tracking due to a large saccade or blink, OCT-PC was signaled to step back 10 B-scans and hold that position until tracking was locked again on target. B-scans collected during tracking failure are removed in post-processing and replaced with rescanned counterparts. (*Top images*) *En face* of all acquired B-scans is shown. This includes B-scans acquired during large saccades or blinks. The blink can be seen as a black line in the upper left image. (*Bottom images*) Motion or blink corrupted B-scans are removed from the volume data set. The black line caused by the blink is gone and several large saccades are also removed. Scale bars indicate 1 deg.

In addition, a fly-through video of the ONH along the axial direction was made. To reduce speckle noise, 4 volume data sets from the same location were compounded together with image registration and then averaged to produce a high quality movie from the ONH. From this movie, C-scans from 4 different depths are shown in Fig. 11. The depths of the C-scans are indicated in a B-scan with colored lines. The fly-through video can be downloaded from the caption in Fig. 11.

The high SNR, the small roll-off (6 dB at 4.2 mm depth [28]) and the use of 1050 nm wavelength provide a deep penetration into the tissue and the mesh-like structure of the lamina cribrosa is clearly resolvable in all depth slices. With tracking, we were able to visualize the porous structure of lamina cribrosa at larger depths, approximately 430 µm below the bottom of the ONH cup (indicated by a white dashed line in Fig. 10). In addition to accurate volume averaging, tracking minimizes the motion artifacts effectively and this is seen as a high quality in the obtained C-scans. The features seen in the C-scans are consistent with the known anatomy of the optic disc [36,37]
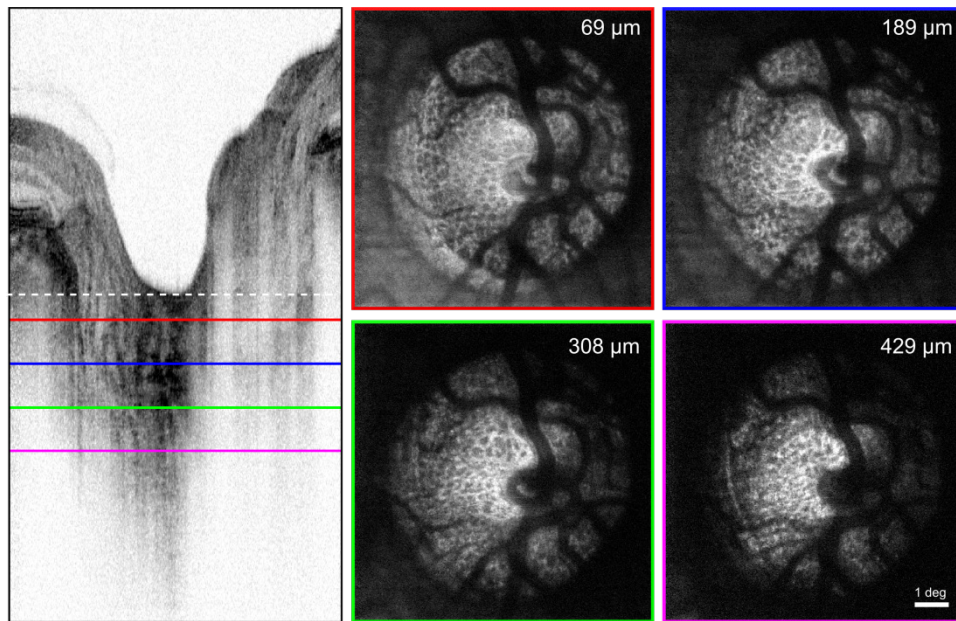

Fig. 11. C-scans extracted from different depths from the ONH movie (Low resolution: Media 1 (3.9 MB), High resolution: Media 2 (17 MB)). Four different data sets were compounded together via image registration to enhance the SNR. The laminar cribrosa mesh-like structure is clearly seen in all selected depths and the pore size increases when moving further away from the center of the optic disc. On the left of the figure, a B-scan is shown to illustrate at which depth each slice (C-scan) was taken (white dashed line indicates the reference point). The porous structure of lamina cribrosa is still visible even at depth of 429 µm measured from the bottom of the ONH cup.

4. Discussion

To summarize the results, we were able to reduce the motion from 17.4 to 0.40 minutes of arc in a model eye and from 7.3 arcmin to 0.32 arcmin in a real eye in OCT images by using the TSLO. The real eye residual SD motion value is less than a third of the theoretical OCT spot diameter on the retina. Without using the validity signal, we were able to track drift and small saccades properly. After implementing the validity signal, locations with large saccades and blinks were rescanned. This allowed the gathering of data sets without gaps and minimal artifacts from tracking failures.

Tracking OCT can be advantageous for routine clinical use, but also for patients who have weakened fixation capabilities due to a disease, age or recent trauma in the eye. Tracking may be most useful for advanced OCT applications such as Doppler OCT [38] (for imaging the vasculature) and polarization-sensitive OCT [39] because it allows one to record or integrate motion-corrected data over long time periods. Since the scanning grid is locked on target, several volume data sets can be taken from the same area and averaged to reduce the speckle noise. Moreover, adaptive optics OCT can greatly benefit from tracking since it is known to be vulnerable to eye motion because of the small field size [40].

Several factors limit the performance of the system and are described here.

Latency: The 2.5 ms latency between measurement and scanner correction has a significant impact on tracking performance. In fact, frequencies above 64 Hz eye motion errors would get amplified. To improve the tracking bandwidth to cover the range of typical saccades and prevent eye motion amplification at frequencies above 64 Hz, latency should be decreased.

Vertical motion: If the eye moves too far vertically, there will be strips from the top or bottom of the current TSLO frame that do not overlap with the reference frame, resulting in a loss of valid tracking signal. In the current implementation, the TSLO system extrapolates the estimate of eye position during these periods from the last valid measure as well as generates an invalid tracking signal.

Reference frame distortion: Every frame in the TSLO video is distorted from eye motion, including the reference frame. If the reference frame contains distortions from a large saccade, the stabilization will continuously fail. Small distortions in the reference frame often enable good stabilization but the distortions give rise to periodic motion artifacts in the eye trace at the frame rate (30 Hz) and subsequently to the OCT scanner. Reselecting the reference frame will often minimize this problem.

Torsion: The TSLO does not measure rotation of the eye around its optical axis, or torsion. Torsional movements of the eye during tracking also give rise to periodic eye motion artifacts at the frame rate (30 Hz). Torsional eye motion in a fixating eye has a standard deviation of less than 0.25 degrees [41] and so has a relatively small effect on the tracking signal.

Every listed factor limits the system in a different way. Vertical and torsional eye movements may or may not be a problem, depending on the subject. Reference frame distortions can be minimized to a negligible level with careful selection by a trained operator. The latency is the dominant source of tracking error and can only be corrected by improvements in software and hardware.

5. Conclusion

In conclusion, we have demonstrated the integration of an experimental SLO eye tracker to our existing OFDI system.

The correction bandwidth of the TOCT system was measured to be 32 Hz. This bandwidth was enough to compensate the majority of the eye motion. In addition to the tracking feature, a validity signal was implemented to the TSLO system to indicate if the tracking lock fails. Locations with invalid signal were rescanned thus B-scans containing rapid saccades and blinks could be discarded from the raw data. The system generates OCT images that have minimal amount of artifacts from drifts, micro saccades and blinks.

Acknowledgments